Estimates of global multicomponent aerosol optical depth and direct radiative perturbation in the Laboratoire de Météorologie Dynamique general circulation model

M. Shekar Reddy,[1] Olivier Boucher,[1] Nicolas Bellouin,[1] Michael Schulz,[2] Yves Balkanski,[2] Jean-Louis Dufresne,[3] and Mai Pham[4]

[1] The global cycle of multicomponent aerosols including sulfate, black carbon (BC), organic matter (OM), mineral dust, and sea salt is simulated in the Laboratoire de Météorologie Dynamique general circulation model (LMDZT GCM). The seasonal open biomass burning emissions for simulation years 2000–2001 are scaled from climatological emissions in proportion to satellite detected fire counts. The emissions of dust and sea salt are parameterized online in the model. The comparison of model-predicted monthly mean aerosol optical depth (AOD) at 500 nm with Aerosol Robotic Network (AERONET) shows good agreement with a correlation coefficient of $0.57(N = 1324)$ and 76% of data points falling within a factor of 2 deviation. The correlation coefficient for daily mean values drops to 0.49 ($N = 23,680$). The absorption AOD (τ_a at 670 nm) estimated in the model is poorly correlated with measurements ($r = 0.27$, $N = 349$). It is biased low by 24% as compared to AERONET. The model reproduces the prominent features in the monthly mean AOD retrievals from Moderate Resolution Imaging Spectroradiometer (MODIS). The agreement between the model and MODIS is better over source and outflow regions (i.e., within a factor of 2). There is an underestimation of the model by up to a factor of 3 to 5 over some remote oceans. The largest contribution to global annual average AOD (0.12 at 550 nm) is from sulfate (0.043 or 35%), followed by sea salt (0.027 or 23%), dust (0.026 or 22%), OM (0.021 or 17%), and BC (0.004 or 3%). The atmospheric aerosol absorption is predominantly contributed by BC and is about 3% of the total AOD. The globally and annually averaged shortwave (SW) direct aerosol radiative perturbation (DARP) in clear-sky conditions is -2.17 Wm^{-2} and is about a factor of 2 larger than in all-sky conditions (-1.04 Wm^{-2}). The net DARP (SW + LW) by all aerosols is -1.46 and -0.59 Wm^{-2} in clear- and all-sky conditions, respectively. Use of realistic, less absorbing in SW, optical properties for dust results in negative forcing over the dust-dominated regions.

1. Introduction

[2] Well-mixed greenhouse gases exert a positive radiative forcing of 2.4 Wm^{-2} in 2000 compared to preindustrial times [*Intergovernmental Panel on Climate Change (IPCC)*, 2001]. It has been established that atmospheric aerosols also play an important role in the global climate change, with a significant but highly uncertain negative radiative forcing. Estimating aerosol effects on the radiation budget to a better accuracy is an important step toward minimizing the uncertainties in assessment of global climate change and there is a need to do so from direct modeling studies [*Anderson et al.*, 2003].

[3] The first multicomponent global aerosol composition and aerosol optical depth (AOD) was presented by *Tegen et al.* [1997] by collating the results from different individual aerosol transport models. Over the recent years several global models have incorporated multicomponent aerosols

[1]Laboratoire d'Optique Atmosphérique, Centre National de la Recherche Scientifique, Université des Sciences et Technologies de Lille, Villeneuve d'Ascq, France.

[2]Laboratoire des Sciences, Climat et de l'Environnement, Gif-sur-Yvette, France.

[3]Laboratoire de Météorologie Dynamique, Centre National de la Recherche Scientifique, Université Paris 6, Paris, France.

[4]Service d'Aéronomie, Université Pierre et Marie Curie, Paris, France.

addressing different facets of aerosol-climate interactions [*Liao et al.*, 2004; *Jacobson*, 2001; *Takemura et al.*, 2002; *Chin et al.*, 2002; *Chuang et al.*, 2002]. Some of the studies are limited to the estimation of AODs while others extend to species-wise aerosol radiative forcing. One of the challenges to the aerosol modeling studies is the evaluation of model performance against measurements which are limited in space and time. The growth of Aerosol Robotic Network (AERONET) providing aerosol data at more than 300 stations all over the world makes it possible to evaluate the models in various regions and at different timescales. In addition aerosol products from various satellite instruments such as Moderate Resolution Imaging Spectroradiometer (MODIS) provide an opportunity for validating the models over the ocean as well as over land.

[4] In this study we present a global multicomponent aerosol simulation from the Laboratoire de Météorologie Dynamique General Circulation Model (LMDZT GCM). The current version of the model includes all major tropospheric aerosol species namely sulfate, black carbon (BC), organic matter (OM), dust, and sea salt. The present study has similarities to some of the previous modeling studies, with some differences and unique features. We represent the seasonal to interannual variability in open biomass burning emissions. The performance of the model is thoroughly evaluated by comparing modeled AODs with AERONET measurements in different regions representing sites dominated by various aerosol types. In addition monthly mean global AOD distributions are compared with MODIS retrievals both over land and ocean. We also compare aerosol absorption with AERONET measurements. Rather than radiative forcing (RF) which strictly speaking applies only to external perturbations, we focus here on the direct aerosol radiative perturbation (DARP) which extends the concept of RF to any aerosol type (i.e., natural and anthropogenic). We present an estimate of the seasonal DARP in the shortwave (SW) and longwave (LW) spectrums at top of the atmosphere (TOA) for clear- and all-sky conditions.

2. Description of the LMDZT GCM

2.1. General Description

[5] The three-dimensional global cycle of major aerosol types is simulated in the LMDZT GCM (version 3.3). Detailed description of most of the model components have been presented in previous works [*Boucher and Pham*, 2002; *Boucher et al.*, 2002; *Reddy and Boucher*, 2004; *Reddy et al.*, 2004; *Hauglustaine et al.*, 2004]. Here we present a brief summary of the various model components. The model is a grid point model with a resolution of 3.75° in longitude and 2.5° in latitude (corresponding roughly to the resolution of a T48 spectral model (F. Hourdin, personal communication, 2004)). It has 19 vertical layers in hybrid sigma pressure coordinate, with 6 layers below about 600 hPa and 9 layers above about 250 hPa. The atmospheric transport is computed with a finite volume transport scheme for large-scale advection [*van Leer*, 1977; *Hourdin and Armangaud*, 1999], a scheme for turbulent mixing in the boundary layer, and a mass flux scheme for convection [*Tiedtke*, 1989]. The time step is three minutes for resolving the dynamical part of the primitive equations. Mass fluxes

are cumulated over five time steps so that large-scale advection is applied every 15 min. The physical and chemical parameterizations are applied every 10 time steps (i.e., every 30 min). The different processes are handled through operator splitting.

[6] Horizontal model winds were nudged to 6 hourly winds from ECMWF analyses with a relaxation time of 0.1 days [*Hauglustaine et al.*, 2004]. This ensures that the model transport is reasonably constrained by ECMWF meteorology while other dynamical and physical processes are driven by the model parameterizations. Simulations are carried out for the years 2000 and 2001 after two months of spin up.

2.2. Sulfate

[7] Our sulfur scheme considers DMS, SO_2, H_2S, DMSO, MSA, and sulfate. The sulfur emissions from fossil fuel combustion and industrial processes are from EDGAR database version 3.0 [*Olivier and Berdowski*, 2001]. A fixed percentage of 5% sulfur from combustion sources is assumed to be directly emitted as sulfate. There is a small additional source of sulfur under of the form of anthropogenic H_2S. The sulfur emissions from biomass and natural (biogenic and volcanic) sources are same as described in the work of *Boucher et al.* [2002]. Aqueous phase reactions include oxidation of SO_2 by H_2O_2 and O_3. In addition sulfate is also formed through gas phase oxidation by OH. The reactions are driven by the prescribed oxidant concentrations from IMAGES model [*Pham et al.*, 1996], except for H_2O_2 which is a prognostic variable with source and sink terms calculated from prescribed OH, HO_2, and photodissociation rates. Full description of the sulfur cycle in the LMDZT GCM, extensive validation and DARP estimates are presented in the work of *Boucher et al.* [2002] and *Boucher and Pham* [2002].

2.3. Carbonaceous Aerosols

[8] Carbonaceous aerosols are of two types namely BC and organic carbon (OC). Black carbon is emitted only from combustion sources, while OC emissions include combustion as well as natural biogenic sources. Fossil fuel and biomass burning contribute about equally to the BC emissions, while OC is predominantly emitted from biomass burning with contributions from fossil fuel combustion and biogenic sources. Emissions of BC and OC from fossil fuel sources are from *Cooke et al.* [1999]. The BC emissions from biomass burning are from *Cooke and Wilson* [1996]. The OC emissions from all types of biomass burning sources are derived by assuming an OC to BC ratio of 7.0, a value within the range used by *Liousse et al.* [1996] and *Chin et al.* [2002]. The OC to BC ratio may vary for different biomass types, which introduces some uncertainty in the OC emissions from biomass burning sources. The magnitude and seasonality of open biomass burning emissions may vary from year to year in different regions. To account for these variations emissions are scaled to satellite measured (ATSR-2) fire counts [*Reddy and Boucher*, 2004]. Natural OC emissions include condensation of volatile organic compounds (VOCs) emitted from biogenic sources. In this study we include secondary OC from terpens by assuming a conversion rate of 11% of terpene emissions from seasonal terpen emission distributions of *Guenther et*

al. [1995]. The conversion rate of 11% is within the experimental range determined by Pandis et al. [1991]. This results in natural OM emissions of 13.9 Tg yr^{-1}. Note that there is a very large uncertainty here since Tsigaridis and Kanakidou [2003] have estimated the global annual SOA production from biogenic production to range from 2.5 to 44.5 Tg OM yr^{-1}.

[9] Oxygen, hydrogen, and other chemical species are always associated with OC, and the resulting aerosol is called organic matter (OM). We use here an OM to OC ratio of 1.4 and 1.6 for fossil fuel and biomass burning sources, respectively [Turpin and Lim, 2002; Reddy and Boucher, 2004]. Carbonaceous aerosols are predominantly emitted in the hydrophobic form, but some fraction of the emissions may be in hydrophilic form as well. Here we assume that BC emissions occur as 80% hydrophobic and 20% hydrophilic, whereas OM emissions occur as 50% hydrophobic and hydrophilic. The aging process of BC and OM is represented by a transfer of the hydrophobic to hydrophilic form with an exponential lifetime of 1.63 days [Reddy and Boucher, 2004].

2.4. Dust

[10] Dust emissions in the model follow Schulz et al. [1998] and Guelle et al. [2000]. The dust fluxes are calculated as a function of soil threshold velocity and wind friction velocities, which are in turn parameterized as a function of the soil particle size and the surface roughness length. Then the dust emission fluxes are determined according to the clay content of eroding soil. This formulation has shown to give very good agreement with measurements of dust mass concentrations and AODs in previous global modeling studies [Schulz et al., 1998; Guelle et al., 2000]. To account for the high spatial variability in horizontal wind speeds, dust emission fluxes have been generated off line using ECMWF 6-hourly horizontal 10-m wind speeds at a resolution of 1.125° × 1.125° and are regridded to the model resolution of 3.75° × 2.5°. These off-line dust emission fluxes are masked online in the model if there is humidity in the soil, which is estimated through a simple bucket equation. We use a bin approach for dust with two bins corresponding to submicron and supermicron particles ($r < 0.5$ and $r > 0.5$ μm, respectively).

2.5. Sea Salt

[11] Sea salt is generated over the open oceans with a large dependence on surface wind speed. Sea salt is predominantly produced from the direct mechanism of entrained air bubbles bursting during whitecap formation due to surface winds [Monahan et al., 1986]. Indirect mechanisms, such as spume and surfing, contribute small amounts of sea salt emissions in comparison to bubble bursting. In the model sea salt emissions are generated using the source formulation of Monahan et al. [1986] along with model 10-m winds according to the following equation:

$$\frac{dF_0}{dr_{80}} = 1.373 \ u_{10}^{3.41} \ r_{80}^{-3} \left(1 + 0.057 r_{80}^{1.05}\right) \times 10^{1.19 \ e^{-B^2}}, \quad (1)$$

where $B = (0.380 - \log r)/0.0650$, dF_0/dr is the number of droplets per unit area of sea surface per increment of

radius (μm), r_{80} is the particle radius (μm) at 80% relative humidity (RH), and u_{10} is the 10-m wind speed (ms^{-1}). Emissions of sea salt cover a range of r_{80} from 0.03 to 20 μm in 10 size bins. In each size bin, emissions are calculated by integrating equation (1) between the bin limits (0.03–0.06, 0.06–0.13, 0.13–0.25, 0.25–0.5, 0.5–1.0, 1.0–2.0, 2–5, 5–10, 10–15, and 15–20 μm). The above formulation was derived from the observations of particles of size between 0.2 to 8.0 μm at 80% RH. Here we extend this parameterization to 20 μm. This extension to large particle size has not shown to create any problem [Gong et al., 2003] and the contribution of this extra bin to AOD is small anyway. Predicted bin-wise aerosol number fluxes are translated to mass fluxes assuming a sea salt mass density of 1.182 g cm^{-3} at 80% RH [Tang, 1997].

2.6. Aerosol Treatment

[12] Aerosols and precursors are released at different altitudes depending on the source type. Emissions from fossil fuel combustion at large point sources (LPS), usually using tall stacks, are released in the model second layer. Large-scale open biomass burning emissions are known to be released at higher altitudes due to thermal buoyancy and are therefore emitted in the model layers 3 to 5, corresponding roughly to heights ranging from 350 to 1500 m. Emissions from all other sources are emitted near the surface.

[13] Once aerosols are released or formed in the atmosphere, they are subject to transport, dry deposition, sedimentation (i.e., gravitational settling), and wet scavenging. Particle size distribution is resolved for all processes using a bin approach for dust (2 bins) and sea salt (10 bins). Here, we do not account for aerosol coagulation in the model. Aerosol dry deposition flux to the ground is calculated as the product of mass concentration in the lowest model layer and the prescribed dry deposition velocity (Table 1). Carbonaceous aerosols are not differentiated between the hydrophobic and hydrophilic forms as far as dry deposition is concerned. Sea salt and dust are also removed from the atmosphere by sedimentation because of their large particle size. Aerosol sedimentation is parameterized using Stoke's law. While calculating the sedimentation velocities for sea salt changes in the particle size and mass densities as a function of atmospheric RH are accounted for according to Tang [1997].

[14] Wet deposition (or scavenging) is treated separately for stratiform and convective precipitation and differently for different aerosols. In-cloud scavenging is parameterized similarly to Giorgi and Chameides [1986]. The fraction of chemical species in the aqueous phase vary for different aerosol types (see Table 1). The hydrophobic carbonaceous aerosols are not allowed to be deposited through in-cloud scavenging. Below-cloud scavenging is parameterized by integrating over the population of raindrops the volume of space that is swept by a raindrop during its fallout. Below-cloud scavenging is applied to both hydrophobic and hydrophilic carbonaceous aerosols in the same manner. In addition, a fraction of the soluble tracers (χ) is scavenged during convective transport (Table 1). The aerosol deposition parameterization is detailed in the work of Boucher et al. [2002].

Table 1. Aerosol Deposition Properties[a]

Parameter	v_d, cm s^{-1}	f	χ
Sulfate	0.05[b], 0.25[c]	0.7	0.5
Hydrophobic BC	0.10	0.0	0.2
Hydrophilic BC	0.10	0.7	0.5
Hydrophobic OM	0.10	0.0	0.2
Hydrophilic OM	0.10	0.7	0.5
Mineral dust, ≤ 1 μm	0.02	0.7	0.2
Mineral dust, $1-10$ μm	1.20	0.7	0.2
Sea salt, ≤ 1 μm	1.10	0.7	0.5
Sea salt, > 1 μm	$1.20-1.50$	0.7	0.5

[a]Here v_d is dry deposition velocity; f is fraction of aerosols in aqueous phase for in-cloud scavenging; χ is fraction of detrained aerosols which is considered as scavenged during convective transport;

[b]is for the oceans;

[c]is for all other surfaces.

2.7. Aerosol Optical Properties and Radiative Forcing

[15] Aerosol optical properties link the atmospheric aerosol loadings to their radiative effects. We assume here that the different aerosol species are externally mixed. Aerosol optical properties (mass extinction coefficient, α_e, single scattering albedo (SSA), ω, and asymmetry factor, g) are computed using Mie theory assuming prescribed lognormal size distributions and refractive indices (Table 2). The size distribution and refractive index in the shortwave range are from *Boucher and Anderson* [1995] for sulfate and from the Global Aerosol Data Set (GADS) for BC [*Köpke et al.*, 1997]. For OM we assume a typical size distribution similar to that of sulfate aerosols and a refractive index from *Köpke et al.* [1997]. In case of dust we use the size distribution properties of *Guelle et al.* [2000] with spectrally varying refractive indices in the shortwave from AERONET measurements [*Dubovik et al.*, 2002]. For sea salt, we employ the size distribution of *O'Dowd et al.* [1997] with refractive index in the shortwave range from the GACP database [Lacis et al., Parameterization of relative humidity effects of hydrophobic aerosols in a climate GCM, http://gacp.giss.

nasa.gov/data_sets/lacis/database.html]. Depending upon their chemical nature, aerosols take up the water and grow in size with increasing RH. We consider RH effect on particle size for the hygroscopic aerosols, sulfate, hydrophilic OM, and sea salt. Hygroscopic growth of sulfate and sea salt particle size is parameterized according to *Tang and Munkelwitz* [1994] and *Tang* [1997], respectively. In the absence of reliable data for OM, we use the hygroscopic growth of sulfate. The refractive index for the hydrophilic aerosols at a given RH is computed as a volume weighted average of the respective aerosol and water refractive indices. We use the model clear-sky RH with a maximum value at 95% as far as aerosol growth factor is concerned.

[16] Aerosol mass extinction coefficient as a function of wavelength is shown in Figure 1 at different RH. At 550 nm α_e for sulfate, hydrophilic OM, and sea salt at 80–95% RH is 4–7 times larger than for the dry aerosols. The wavelength dependence of α_e is larger for aerosols with smaller size (e.g., BC, OM, and sulfate) as compared to aerosols with larger size (e.g., supermicron sea salt and dust). It is important to note that dust SSA at 550 nm comes at 0.99 and 0.95 for the submicron and supermicron size ranges, respectively, which is larger than the values employed in some of the previous global aerosol models [e.g., *Takemura et al.*, 2002]. This larger dust SSA has been confirmed by various studies [*Kaufman et al.*, 2001; *Clarke et al.*, 2001; *Haywood et al.*, 2003].

[17] Mie theory is also used to estimate aerosol optical properties in the longwave range. Calculations are done at a high spectral resolution and compressed to the 5 spectral bands of the radiative transfer model by doing a weighted averaged with the Planck emission function at 260 K. Although it is important to account one way or the other for the wavelength dependence of longwave radiation within each wave band, the results are not very sensitive on how this is done (i.e., the choice of the Planck temperature is not very sensitive). Refractive indices in the longwave range are taken from GACP database for hydrated

Table 2. Physical and Optical Properties at 550 nm of the Dry Aerosol[a]

Aerosol Type	ρ, g cm^{-3}	r_0, μm	σ_g	α_e, m^2 g^{-1}	ω	g	Refractive Index
Sulfate	1.769	0.0355	2.0	4.311	1.00	0.609	$1.53-0.000i$
BC	1.000	0.0118	2.0	9.412	0.206	0.335	$1.75-0.45i$
OM	1.769	0.0355	2.0	3.159	0.969	0.542	$1.53-0.005i$
Dust, ≤ 1 μm[b]	2.610	0.29	2.0	2.876	0.991	0.694	$1.48-0.00164i$
Dust, $1-10$ μm[b]	2.610	0.29	2.0	0.557	0.955	0.706	$1.48-0.00164i$
Sea Salt[c]	1.183	0.198, 1.97	1.9, 2.0	–	–	–	$1.516-0.215 \ 10^{-3}i$
(0.03–0.06 μm)				0.279	0.999	0.073	
(0.06–0.13 μm)				1.863	1.000	0.350	
(0.13–0.25 μm)				5.180	1.000	0.685	
(0.25–0.50 μm)				6.305	1.000	0.783	
(0.50–1 μm)				2.274	0.999	0.669	
(1–2 μm)				0.995	0.999	0.780	
(2–5 μm)				0.395	0.997	0.808	
(5–10 μm)				0.190	0.995	0.829	
(10–15 μm)				0.109	0.996	0.838	
(15–20 μm)				0.076	0.995	0.843	

[a]Except for sea salt for which properties are given at 80% RH. Here ρ is density; r_0 is modal radius; σ_g is geometric standard deviation; α_e is mass extinction coefficient; ω is aerosol single scattering albedo; and g is asymmetry factor.

[b]A monomodal lognormal size distribution is used and optical properties are averaged over the two bins corresponding to the submicronic and supermicronic size ranges ($d \leq 1$ and $d > 1$ μm, respectively).

[c]A typical bimodal lognormal size distribution is assumed from *O'Dowd et al.* [1997] in order to integrate sea-salt optical properties over each size bin. The number concentrations for the first and second modes are 70 and 3 cm^{-3}, respectively. Particle size refers to radius at 80% RH.
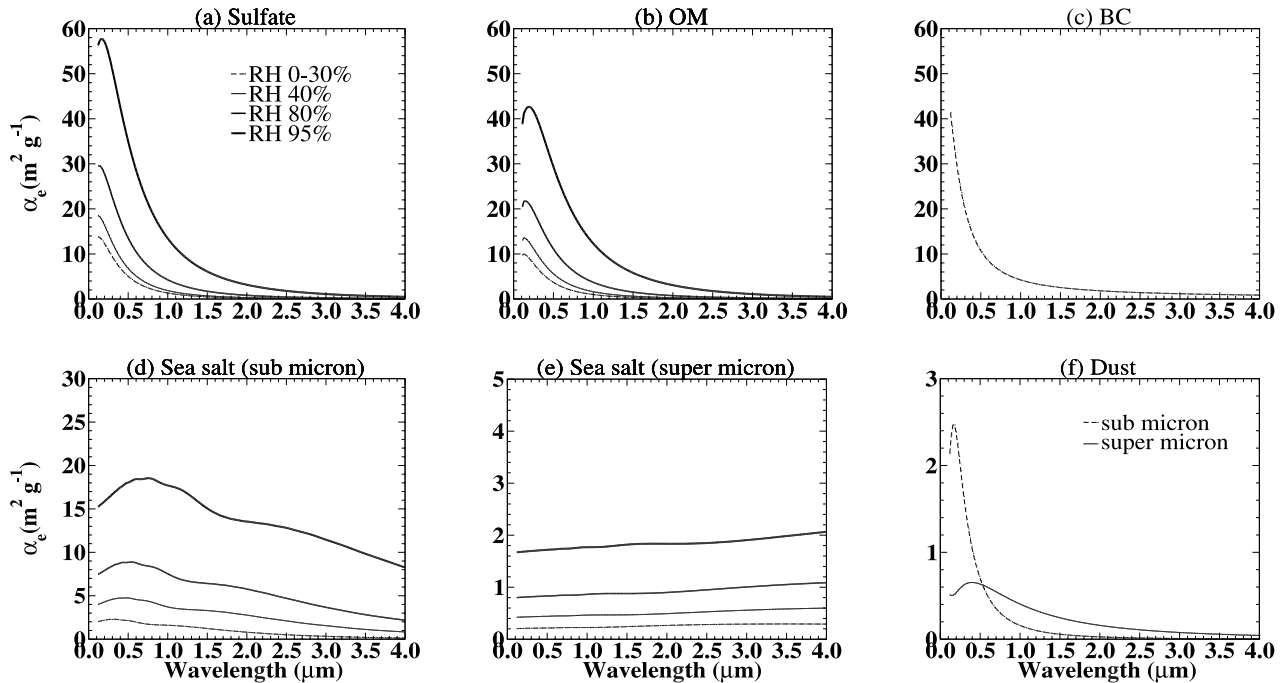
Figure 1. Aerosol mass extinction coefficients (m^2 (g sulfate)$^{-1}$ or m^2 (g dry aerosol)$^{-1}$) for the different aerosol types. For the purpose of this diagram, submicron and supermicron sea salt refers to the averages of bins 1 to 5 and 6 to 10, respectively. See color version of this figure in the HTML.

sulfate and sea salt, OPAC for BC, and *Volz* [1973] for dust. In the absence of data for OM, we assume the same optical properties as of sulfate aerosols.

[18] The radiative code in the LMDZT GCM consists of improved versions of the parameterizations of *Fouquart and Bonnel* [1980] (solar radiation) and *Morcrette* [1991] (terrestrial radiation). The shortwave spectrum is divided into two intervals: $0.25-0.68$ and $0.68-4.00$ μm and longwave spectrum is divided into 5 intervals. The model accounts for

the diurnal cycle of solar radiation and allows fractional cloudiness to form in a grid box. In the cloud-free portion of the grid box the optical properties of aerosols are combined and a delta approximation of the forward scattering peak is made to account for the highly asymmetric aerosol phase function. The reflectivity and transmissivity of a layer are computed using the random overlap assumption [*Morcrette and Fouquart*, 1986] by averaging the clear and cloudy sky fluxes weighted linearly by their respective fractions in the

Table 3. Global Aerosol Budgets in the LMDZT GCM[a]

Aerosol Type	Emissions, Tg yr^{-1}	Dry Deposition,[b] Tg yr^{-1}	Wet Deposition, Tg yr^{-1}	Burden, Tg	Residence Time, days
SO$_2$	108.1[c]	25.6 (24%)[d]	9.0 (8%)[d]	0.39	1.3
Sulfate	69.9[e]	8.0 (11%)	61.9 (89%)	0.73	3.8
BC	10.5	1.7 (16%)	8.8 (84%)	0.19	6.6
OM	90.1	12.6 (14%)	77.5 (86%)	1.75	7.1
Dust	1307	924 (71%)	383 (29%)	12.10	3.4
(≤1 μm)[f]	122	25 (93%)	97 (7%)	3.01	9.0
(> 1 μm)[f]	1185	899 (78%)	286 (22%)	9.09	2.8
Sea salt	3442	2343 (68%)	1098 (32%)	4.62	0.5
(≤1 μm)[g]	78	8 (9%)	70 (91%)	0.41	1.9
(> 1 μm)[g]	3363	2335 (69%)	1028 (31%)	4.21	0.5

[a]The unit Tg is Tg S for sulfate and SO$_2$, Tg BC for BC, Tg dry OM for OM, Tg dust for dust, and Tg dry sea salt for sea salt.

[b]Dry deposition also includes sedimentation for dust and sea salt.

[c]SO$_2$ sources include the direct emissions from combustion and oxidation of sulfur compounds in the atmosphere.

[d]Additional sink to SO$_2$ is transformation to sulfate in the atmosphere.

[e]Sulfate sources include the direct emissions from combustion (about 3.65 Tg S yr^{-1}) and oxidation of SO$_2$ in the atmosphere.

[f]Refers to particle diameter.

[g]Refers to bins $1-5$ and $6-10$, respectively.
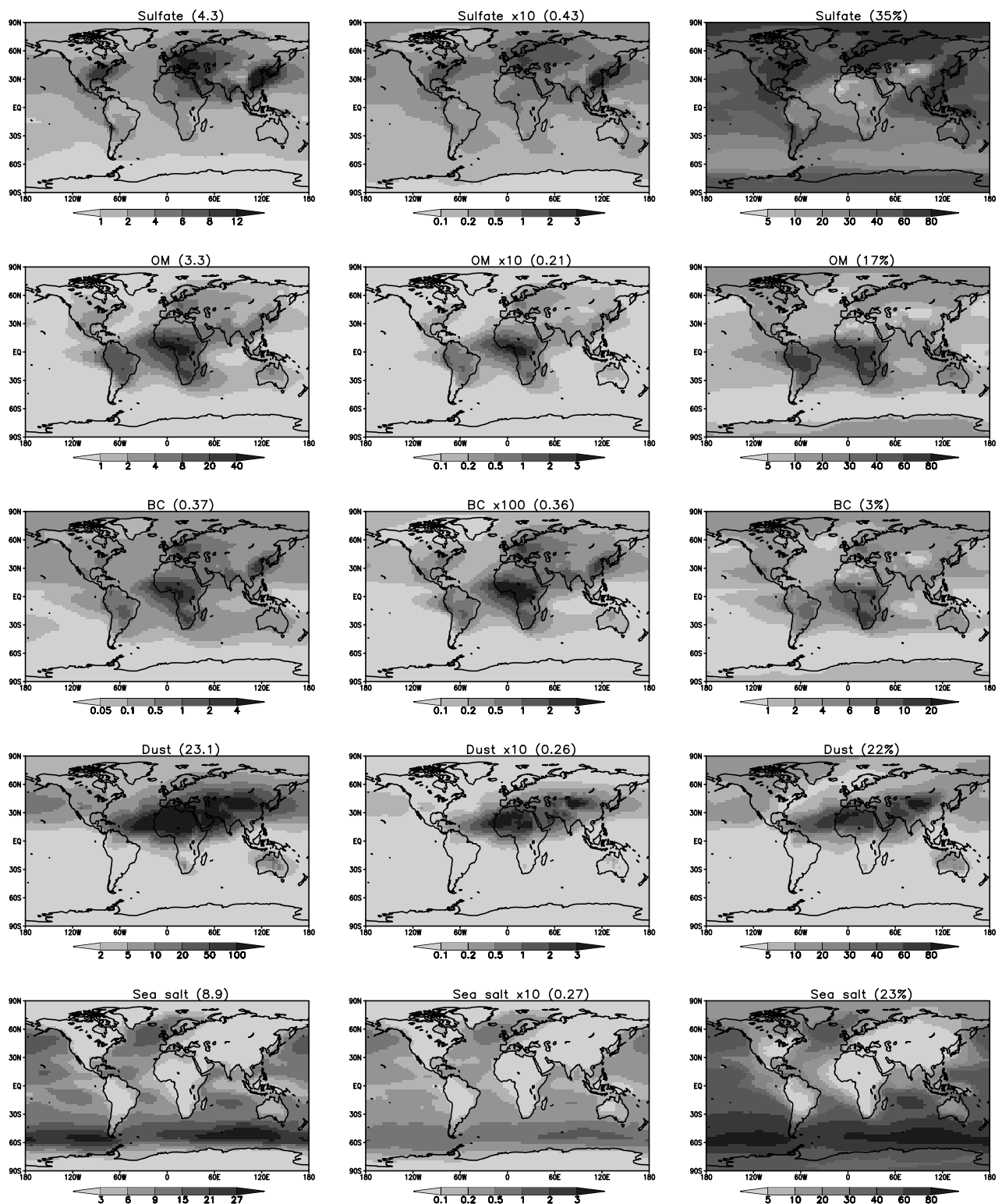
Figure 2. Distributions of annually averaged dry aerosol burden (mg m^{-2}, left panels), aerosol optical depth at 550 nm (dimensionless, middle panels), and contribution of individual species to total AOD at 550 nm (percent, right panels). The values in parenthesis are the global annual averages of the respective quantities. Note that scales are different on all plots. See color version of this figure in the HTML.
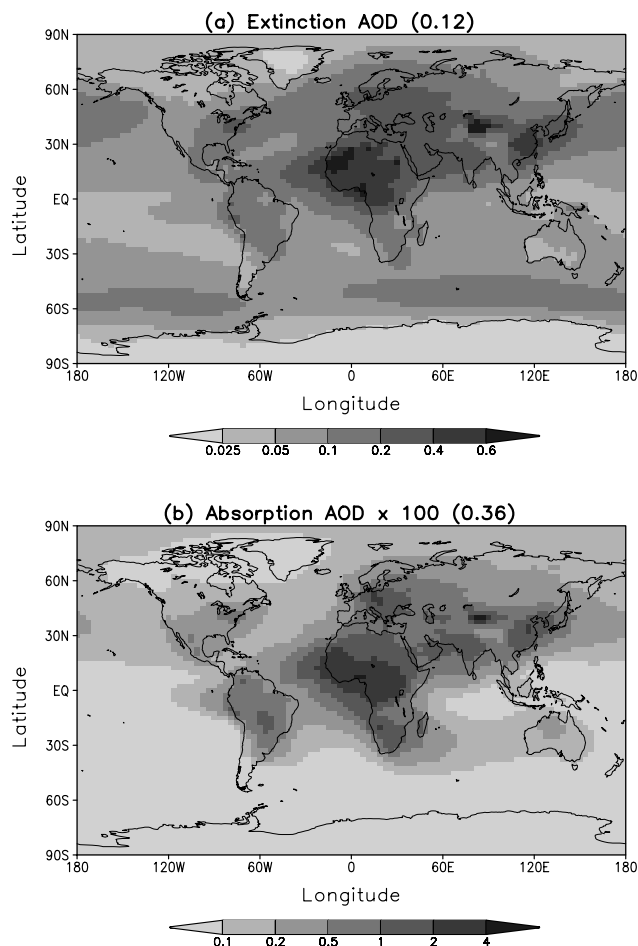
Figure 3. Distribution of the annually averaged AOD at 550 nm for (a) extinction and (b) absorption (×100). See color version of this figure in the HTML.

layer. The radiative fluxes are computed every two hours, at the top-of-atmosphere (TOA) and at the surface, with and without the presence of clouds, and with and without the presence of aerosols. The clear-sky and all-sky aerosol radiative forcings can then be estimated as the differences in radiative fluxes with and without aerosols.

3. Global Aerosol Distributions

[19] The global annual aerosol budgets are given in Table 3. The atmospheric fates of sulfate, BC, and OM are primarily controlled by wet deposition which accounts for more than 80% of sinks, with dry deposition making the balance. Dust and sea salt are larger in size for which sedimentation and dry deposition represent about 70% of their removal. Sulfate has a residence time of 3.8 days. Carbonaceous aerosols have a residence time of about one week which is the longest among all the aerosol types. Submicronic dust is not removed efficiently neither by wet nor by dry deposition, resulting in a residence time of 9.0 days and the potential for long range transport. Most of the sea salt is concentrated in the supermicronic size range and has the smallest residence time (0.5 days) of all aerosol types.

[20] Surface concentrations of individual species have been evaluated in the work of *Boucher et al.* [2002] for DMS, SO_2, and sulfate and *Reddy and Boucher* [2004] for BC and OM. A comparison of sea salt concentrations with measurements (not shown) shows that the model-predicted seasonal cycle in sea salt concentrations is in general good agreement with measurements at the Mace Head, Heimaey, Cape Grim, Hawaii, and Bermuda stations. However, at Midway, Oahu, Miami, and Barbados the modeled sea salt concentrations are underestimated as compared to the measurements.

[21] The globally and annually averaged distributions of aerosol burdens are shown in Figure 2 (left panels). Sulfate burdens are largest over Europe, east Asia, and the east coast of North America. Carbonaceous aerosols are largest over Africa, with secondary maxima over South America, south Asia, east Asia, and eastern Europe. The dust distribution is characterized by large loadings over the intense source regions of Sahara, west and east Asia. Transport of Saharan dust into the Atlantic Ocean and Asian dust to North America is also noteworthy. The largest sea salt loadings are present in the high southern latitudes, reflecting the large emissions in this region from strong surface winds.

[22] Aerosol optical depths (Figure 2, middle panels) exhibit the same geographical patterns as aerosol burdens. Under the assumption of an external mixture we compute the total AOD as the sum of AODs by the individual species. The total extinction (τ_e) and absorption (τ_a) AOD distributions are shown in Figure 3. The striking feature of the distribution of τ_e is the very large values of 0.5 to 0.7 over the dust and biomass burning regions. There is a secondary maximum of 0.3 to 0.5 over the regions of large fossil fuel and biofuels use. The smallest AODs over land are found over North and South America. The relative contributions of each aerosol species to the total τ_e is also shown in Figure 2 (right panels). Globally averaged contribution to τ_e is largest from sulfate (35%) followed by sea salt (23%), dust (22%), OM (17%), and BC (3%). The sulfate contribution is about 40–50% over North America, eastern Europe, east Asia, and corresponding outflow regions. Carbonaceous aerosols are dominant over Africa and South America with contributions as large as 60–80%. Dust is the main contributor to τ_e over north Africa and the tropical Atlantic Ocean, Arabian Sea, and northern China-Mongolia, with values as large as 60–90%. Sea salt dominates in the 50–70°S latitudinal band contributing 70–90% to τ_e. It is mostly BC which determines the distribution of τ_a although the contributions of OM and dust are also visible in Figure 3b.

4. Comparison to AERONET Measurements
4.1. Extinction Aerosol Optical Depth

[23] Validation of global aerosol models is often challenged by the limited number of observations in space and time. The AERONET network, providing quality-assured data of aerosol parameters at more than 300 locations spread all over the world, bring new opportunities for models validation. To evaluate the present model we compare model-predicted monthly mean τ_e (500 nm) with AERONET retrievals (Figure 4). Model monthly mean values are calculated by averaging values from days for which AERONET
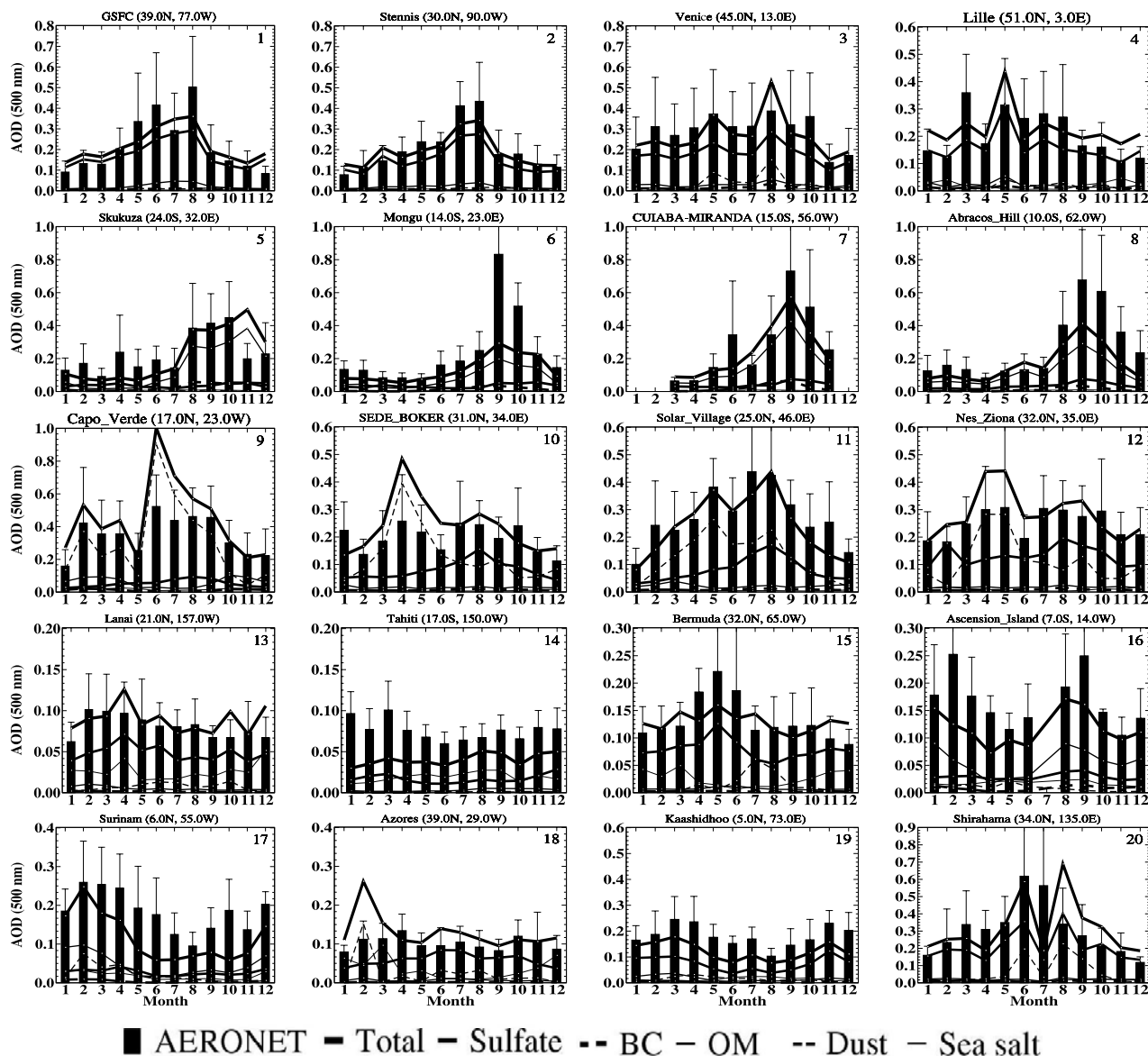
Figure 4. Model and measured AOD at 500 nm at different AERONET sites. The model monthly means are calculated only from days for which AERONET measurements are reported for the years 2000 and 2001. The error bars are ±1 standard deviation around AERONET monthly means. See color version of this figure in the HTML.

retrievals are available during years 2000 and 2001. A set of sites has been selected to represent different geographical regions and aerosol types.

[24] The first set of four sites (Goddard Space Flight Center, Stennis, Venice, and Lille) are mostly influenced by fossil fuel combustion. At all of the sites the model predicts that about 80% of τ_e is from sulfate and associated cations and water. The model-predicted values are within the range of uncertainties of measurements. Sites 5–8 are mainly affected by biomass burning (Skukuza and Mongu in Africa, Cuiba Mirand and Abracos Hill in South America). In Africa biomass burning peaks from August to October and the model shows a corresponding increase in τ_e. However, the peak in the model can be shifted by 1 month compared to observations (e.g., at Skukuza). At Mongu the

modeled τ_e is smaller by a factor of 2 to 4 compared to AERONET during the biomass burning season. At South American sites the seasonal cycle is well reproduced by the model, but with an underestimation of the absolute values of τ_e. The underestimation of emissions of carbonaceous aerosols was discussed in the work of *Reddy and Boucher* [2004] and probably results from an underestimation of the sources. One can also question the representativity of one AERONET site for a model grid box of 3.75° by 2.5° resolution.

[25] The sites affected by dust are numbered 9–12 (e.g., Capo Verde, Sede Boker, Solar Village, and Nes Ziona). Capo Verde is situated off the west coast of Africa and experiences dust from north Africa. The model reproduces correctly the magnitude and seasonal cycle of τ_e at this site.
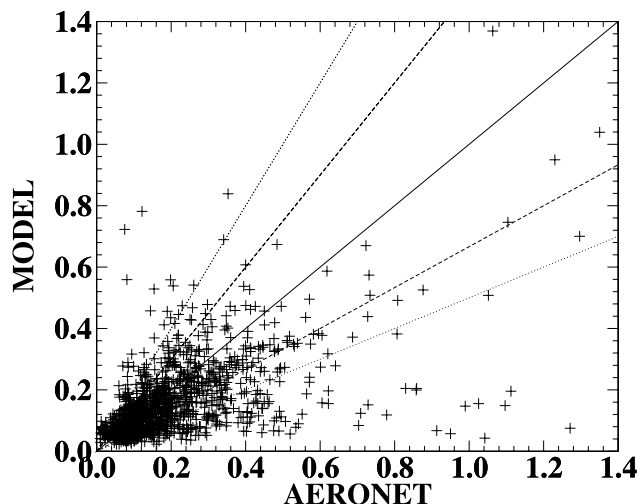
Figure 5. Scatterplot of monthly mean model and AERONET AOD at 500 nm. The solid, dashed, and dotted lines represent the 1:1, 1:1.5 and 1.5:1, and 1:2 and 2:1 lines, respectively.

The Middle East stations of Sede Boker, Solar Village, and Nes Ziona show seasonal cycles in τ_e which is well reproduced by the model but with a slight overestimation of τ_e by 5–25%. At Nes Ziona, sulfate aerosols also contribute significantly to the simulated AODs. Sites 13–16 (e.g., Lanai, Tahiti, Bermuda, and Ascension Island) are island stations and are influenced by marine aerosols (i.e., sea salt and natural sulfur) and long range transport of aerosols from continents. At the Pacific Island stations of Lanai and Tahiti τ_e is mainly made up by sea salt and sulfate. The modeled τ_e is in the uncertainty range of measurements with a bias toward to smaller values at Tahiti. The underestimation at Tahiti could be from too low sea salt emissions in the model. Bermuda is situated downwind of the east coast of the United States and is affected by the marine aerosols in addition to sulfate from North America and dust from north Africa. τ_e is dominated by sulfate throughout the year with a summer peak from dust transported from Africa. Ascension Island is situated on the west coast of South Africa and is affected by sea salt in addition to carbonaceous aerosols transported from Africa. The model predicted seasonal cycle is in agreement with measurements with a magnitude at the lower end of the measurements during the biomass burning season.

[26] Sites 17–20 (e.g., Surinam, Azores, Kaashidhoo, and Shirahama) are located downwind of pollution sources and are mainly influenced by aerosols advected from the continents. Surinam is located to the northeast of South America. The model-predicted seasonality of τ_e is in good agreement with AERONET, but with a too low magnitude during the biomass burning season (September–October). The Azores site is primarily affected by pollution from Europe. In addition Azores also receives dust from Africa during the early part of the year. At the Indian Ocean station of Kaashidoo modeled τ_e is underestimated [*Reddy et al.*, 2004]. Shirahama receives pollution from east Asian countries and τ_e is dominated by sulfate and dust. At this site the modeled τ_e is overestimated during September–

Table 4. Average Model and AERONET AODs in Different Regions of the World

Region	Sample Size (N)[a]	Model τ_e[b]	AERONET τ_e[b]	r[c]
South America	202	0.124 ± 0.083	0.223 ± 0.179	0.52
North America	560	0.130 ± 0.078	0.152 ± 0.109	0.66
Africa	222	0.228 ± 0.172	0.314 ± 0.249	0.51
Europe	73	0.256 ± 0.089	0.231 ± 0.101	0.51
Asia	105	0.219 ± 0.171	0.222 ± 0.129	0.43
Australia	15	0.069 ± 0.017	0.181 ± 0.084	0.34
Remote	147	0.079 ± 0.059	0.087 ± 0.056	0.56
Global	1324	0.153 ± 0.121	0.195 ± 0.166	0.57

[a]Refers to the number of monthly means in 2000 and 2001.
[b]Average and standard deviation AOD computed from monthly means.
[c]Correlation coefficient between monthly mean model and AERONET values.

December probably due to an overestimation of the dust contribution.

[27] It is not possible to show here a comparison between AERONET and modeled AODs for all of the sites but a scatterplot which include all sites with data for the years 2000 and 2001 is shown in Figure 5. The correlation coefficient between monthly mean AERONET and modeled τ_e is 0.57 ($N = 1324$). In a similar study *Chin et al.* [2002] also showed a good agreement between AERONET and modeled τ_e with a correlation coefficient of 0.7 but the analysis was restricted to 20 sites. There are 76% and 54% of the data points falling within a factor of 2 and 1.5 deviations, respectively. The model tends to underestimate τ_e when measured τ_e is larger than 0.6. This is due to months of biomass burning in Africa and South America, where τ_e is systematically underpredicted. The correlation coefficient between daily mean AERONET and modeled τ_e drops to 0.49 ($N = 23,680$) with 65% of data points falling within a factor of 2 deviation. The smaller correlation coefficient for daily averages compared to monthly averages is partially explained by the fact that we lack in the model the daily variability in biomass burning emissions and to some extent fossil fuel combustion.

[28] To gain an understanding of the model performance in the different regions, a comparison between AERONET
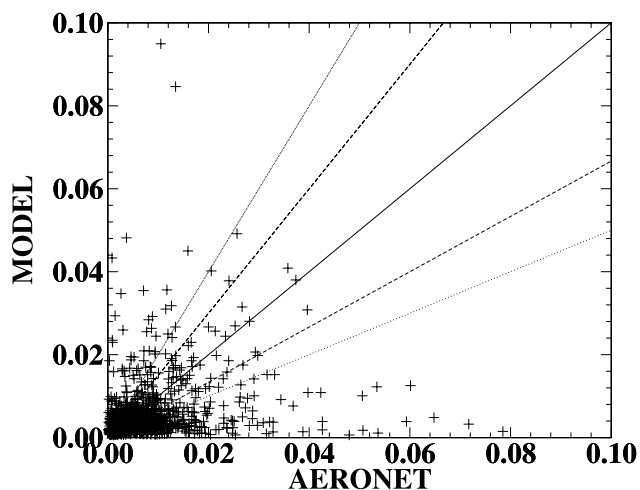
**Figure 6.** Same as Figure 5 but for the absorption AOD at 670 nm.
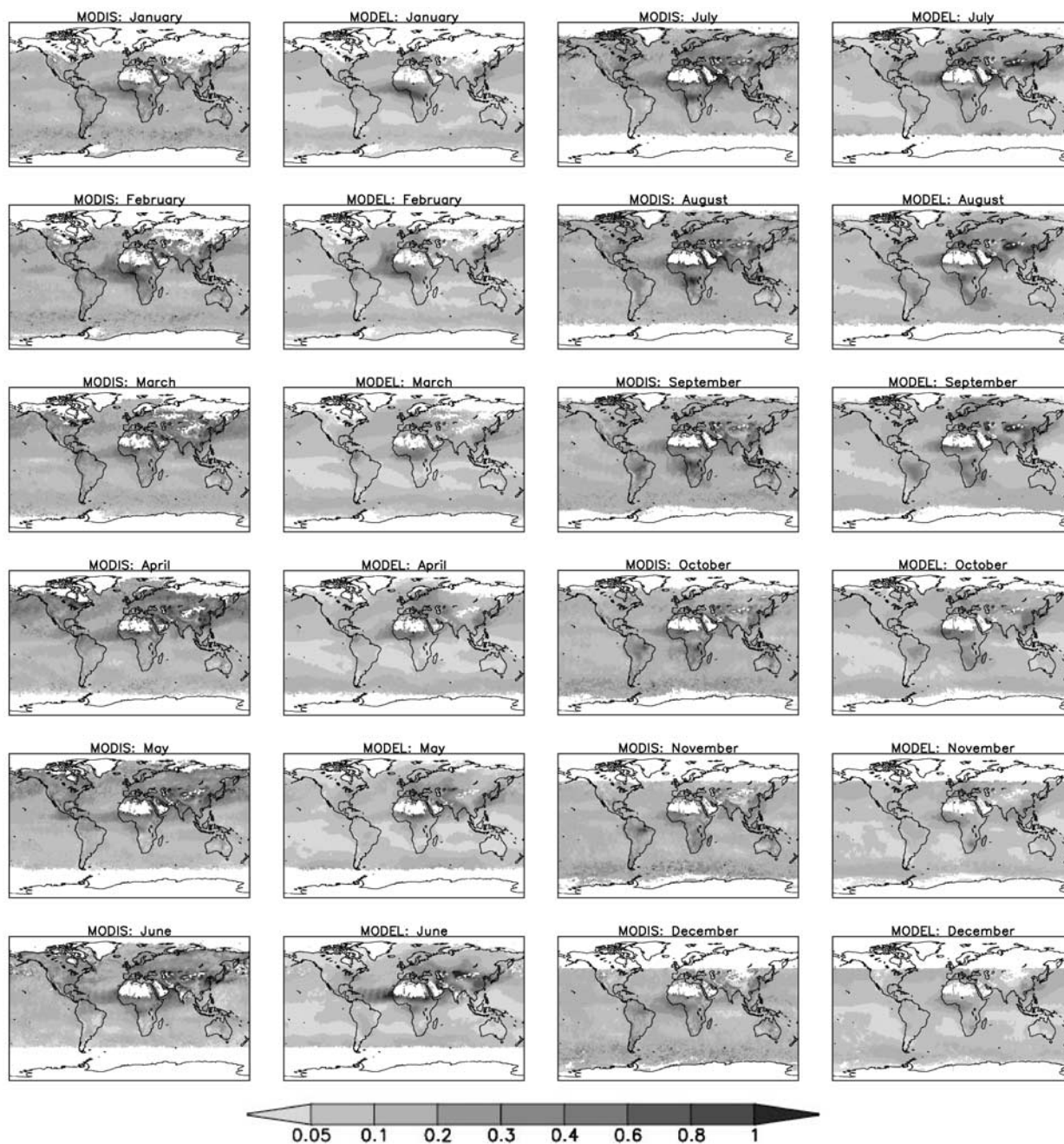
Figure 7. Comparison of monthly mean model and MODIS AOD at 550 nm for the year 2001. The model AOD is sampled according to MODIS daily values. See color version of this figure in the HTML.

and modeled τ_e is performed by geographical region (Table 4). The largest correlation coefficient between AERONET and modeled AODs is over North America (0.66) and the lowest over Australia (0.34) and Asia (0.43). The model underestimates τ_e in all of the regions except over Europe where the emissions may have decreased in between the emission base year and the measurement years. The underestimation ranges from 10 to 62% compared to AERONET. As an average over all stations the model underestimates monthly mean τ_e by 22% compared to AERONET. As AERONET sites are probably biased toward

regions of large AODs this probably corresponds to an upper limit of the model underestimation.

[29] There are other potential reasons for discrepancy between the model and AERONET. There is probably an underestimation of the emission rates of some aerosol species. It should be kept in mind that AERONET measurements are for daytime, cloud-free conditions, while model AODs are for 24-hour all-sky conditions. The uncertainties in the aerosol optical properties, RH, hygroscopic growth also contribute to some of the discrepancy. Especially for biomass burning regions, AERONET stations are located
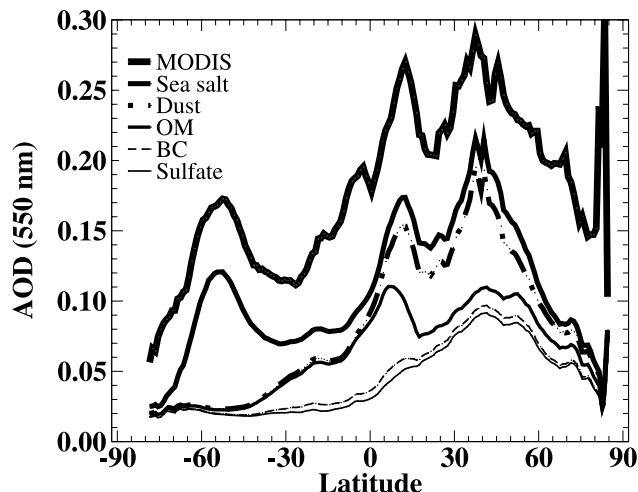
Figure 8. Cumulative species-wise annually and zonally averaged AOD at 550 nm predicted by the model and total AOD retrieved from MODIS data for the year 2001. The model AOD is sampled according to MODIS daily values. See color version of this figure in the HTML.

close to regions of maximum burning while the model may diffuse the source regions too much.

4.2. Absorption Aerosol Optical Depth

[30] There is a recent concern in the literature about underestimation of aerosol absorption in global aerosol models and the implications for global warming. *Sato et al.* [2003] showed a comparison of spectral aerosol absorption optical depth from two global models (GOCART and GISS) and AERONET measurements from about 250 sites around the world. It was concluded that BC absorption in the models has to be increased by a factor 2 to 4 to match AERONET measured aerosol absorption. The same analysis applied to our model shows that a factor of 4 increase in BC absorption would also be required. However the comparison is based on annual mean aerosol absorption optical depth and may be biased toward large aerosol absorption situations. To resolve this apparent discrepancy we compare the model-predicted τ_a (at 670 nm) with AERONET retrievals. The number of retrievals of aerosol absorption is smaller than the number of retrievals of extinction. Aerosol SSA retrievals are not performed at low AODs as these are not reliable [*Dubovik et al.*, 2002]. Here we only consider daily mean τ_a values for which an aerosol SSA is also reported and compute monthly means only from these values for the period of 2000 and 2001 (Figure 6). The AERONET and modeled monthly mean τ_a are poorly correlated with a correlation coefficient of 0.27 ($N = 349$) with 53% of the data points falling within a factor of 2 deviation. The modeled monthly mean τ_a, averaged over AERONET sites, is 0.011 ± 0.012, underestimated by 24% compared to an AERONET mean of 0.015 ± 0.015. If the comparison between modeled and measured τ_a is done on a daily basis the correlation coefficient is 0.29 ($N = 1219$). When considering all of the reported AERONET absorption measurements (i.e., by not masking with aerosol SSA retrievals) the average AERONET monthly mean τ_a is 0.0082 ± 0.0089, almost a factor of 2 smaller than if data are filtered

with SSA retrievals. This clearly demonstrates that the selection of representative data is very important and can make a large difference in the computation of the global mean aerosol absorption. In this case the correlation coefficient between AERONET and modeled τ_a is 0.29 ($N = 974$) and the model average monthly mean τ_a is 0.0063 ± 0.0088 underestimated by 22% compared to AERONET. The present analysis does not support the conclusions of *Sato et al.* [2003] and suggests that the underestimation of aerosol absorption in global aerosols models is real but not as dramatic as reported by *Sato et al.* [2003]. The discrepancy between the two analyses probably arises because of different data samplings in the models.

5. Comparison to Satellite Data

[31] The MODIS instrument onboard the Terra platform has been delivering aerosol products since April 2000. As opposed to other instruments MODIS retrievals are available over both ocean and land with a near global coverage except over bright surfaces. Retrievals of AODs from MODIS are in good agreement with independent ground-based AERONET measurements. The reported errors in the MODIS retrievals of AOD are $\pm 0.05 \pm 0.2 \times$ AOD over land [*Chu et al.*, 2002] and $\pm 0.03 \pm 0.05 \times$ AOD over ocean [*Remer et al.*, 2002]. However the error may be larger over some particular regions. Here we use daily MODIS aerosol products to reconstruct monthly mean fields and sample the model AODs accordingly. The comparison between model and MODIS monthly mean τ_e (550 nm) for the year 2001 is shown in Figure 7. Both the model and MODIS distributions show a large τ_e over central and north Africa. The model underestimates τ_e over South Africa during the biomass burning season implying that emissions are too low in the model. Over South America τ_e is systematically underestimated by the model, in agreement with our previous model evaluation [*Reddy and Boucher*, 2004]. Mineral dust dominates τ_e over the Arabian peninsula and the Gobi desert and there is a good agreement between MODIS and the model. In general the agreement between MODIS and model is better for larger τ_e values compared to smaller values. One of the major discrepancy between the model and satellite distributions is an underestimation of τ_e by the model over Asia. Emissions of anthropogenic carbonaceous aerosols in the model correspond to the mid 1980s while industrial growth and increase in population during the last decade have resulted in an increase in aerosol emissions over Asia and an underestimation of τ_e in the model. Over North America the model consistently underestimates τ_e as compared to MODIS. However we have shown that model predicted sulfate concentrations agree well with observations over the United States [*Boucher et al.*, 2002] while concentrations of OC are underestimated by a factor of 2 to 3 [*Reddy and Boucher*, 2004]. The lower τ_e over North America probably results from an underestimation of the contribution of carbonaceous aerosols rather than sulfate. Over the remote oceans τ_e is contributed primarily by sea salt and is underpredicted by the model by a factor of 3 to 5. This underestimation has a significant impact in terms of aerosol radiative effects.

[32] The zonally and annually averaged τ_e for different aerosol species is shown in Figure 8 along with MODIS
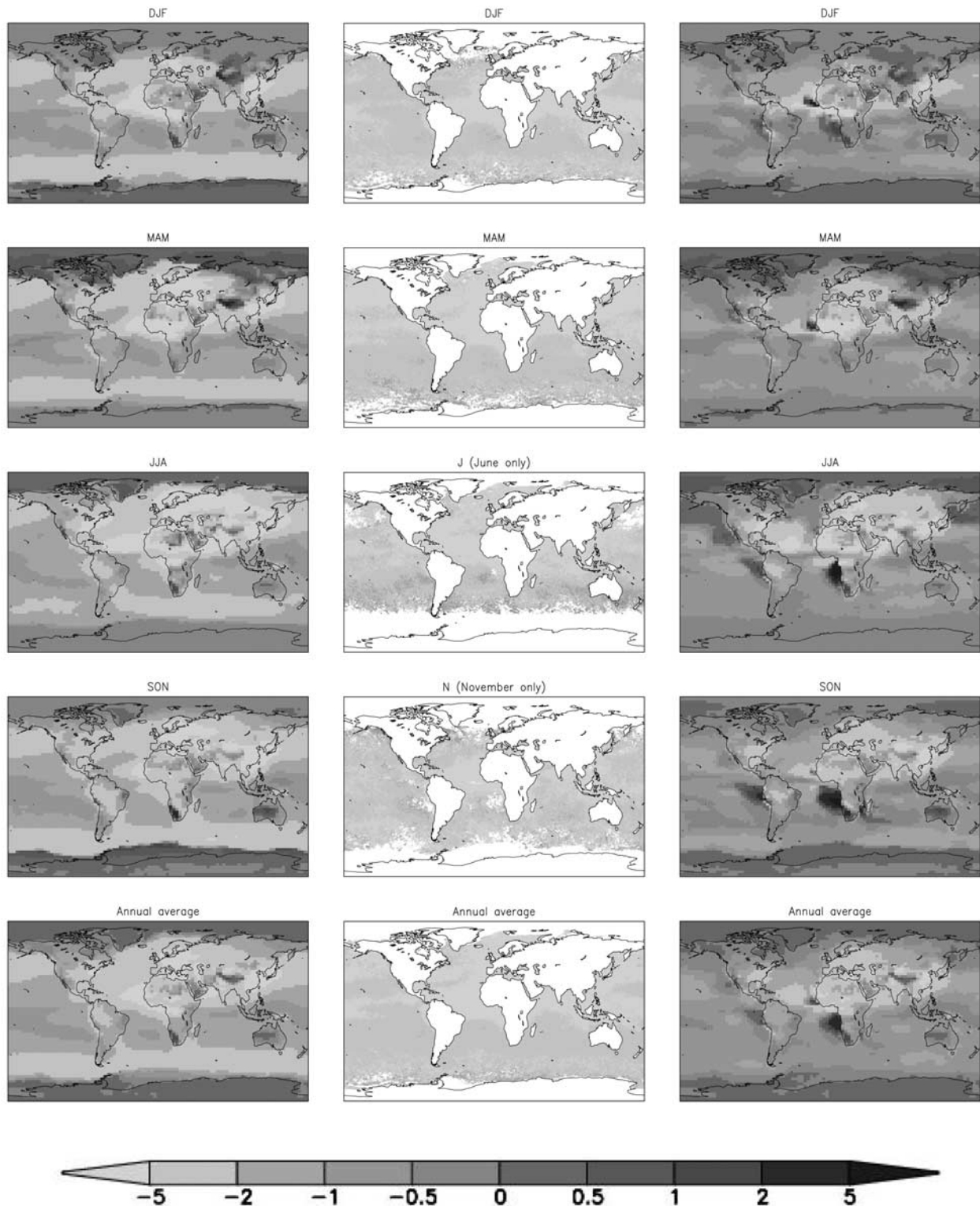
Figure 9. Seasonally and annually averaged DARP (W m^{-2}) in the shortwave spectrum in clear-sky conditions from the model (left panels) and from POLDER (middle panels), and in all-sky conditions from the model (right panels). See color version of this figure at back of this issue.

retrievals. The patterns of the zonal τ_e averages are very similar in MODIS and the model, with a systematic underestimation of the model. The zonally averaged τ_e peaks at about 10°N and 35–50°N in the NH and at about 50°S in the SH. The model peaks coincide with peaks in τ_e by dust (11°N and 36°N), τ_e by sulfate aerosols (35–60°N), and τ_e by sea salt (53°S). AOD by carbonaceous aerosols peaks at about 6°N, where intense sources are located, but does not

Table 5. Clear Sky and All Sky, Hemispheric and Global, Seasonal and Annual Averages of the DARP (Wm^{-2}) in the Shortwave and Longwave Spectrums
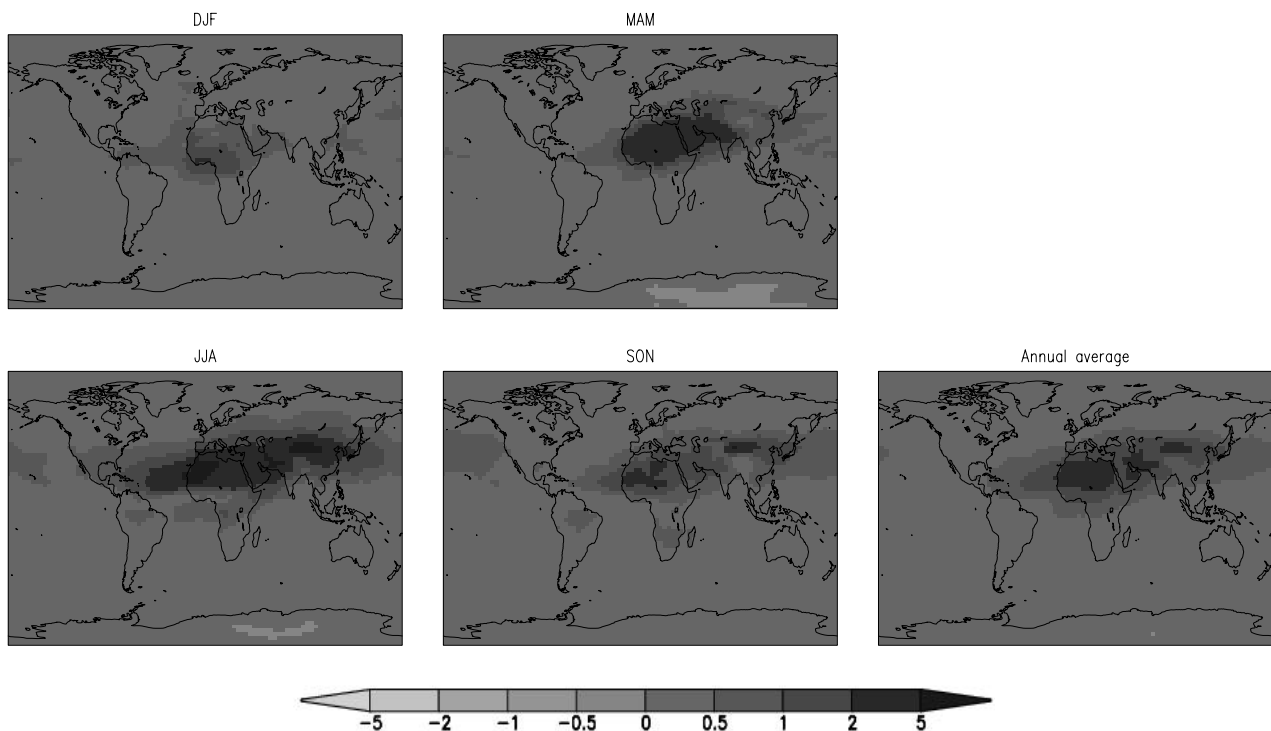
	Shortwave						Longwave					
	Clear Sky			All Sky			Clear Sky			All Sky		
Season	SH	NH	Global	SH	NH	Global	SH	NH	Global	SH	NH	Global
DJF	−1.68	−2.20	−1.94	−0.56	−1.22	−0.89	+0.31	+0.58	+0.44	+0.18	+0.37	+0.27
MAM	−1.46	−2.64	−2.05	−0.67	−1.33	−1.00	+0.37	+1.02	+0.70	+0.21	+0.67	+0.44
JJA	−1.49	−3.61	−2.55	−0.62	−1.98	−1.31	+0.48	+1.60	+1.04	+0.28	+1.10	+0.69
SON	−1.63	−2.70	−2.17	−0.46	−1.52	−0.99	+0.41	+0.86	+0.63	+0.24	+0.58	+0.41
Annual	−1.56	−2.78	−2.17	−0.58	−1.51	−1.04	+0.39	+1.01	+0.71	+0.23	+0.68	+0.45

show up in the zonal average of the total τ_e. The underestimation of τ_e by the model in the SH high latitudes compared to satellite retrievals is a common problem to many of the global aerosol models [*Penner et al.*, 2002]. It is not clear however whether the underestimation is real or whether it is an artifact of the satellite data due to cloud or foam contamination. For example τ_e retrieved from AVHRR using different algorithms differed by a factor of 2 in these regions [*Penner et al.*, 2002]. Different satellite retrievals show a large scatter in the latitudinal band of 50–70°S, with POLDER being the lowest (about 0.05) and *Higurashi et al.* [2000] retrievals of AVHRR being the largest (about 0.2) [*Myhre et al.*, 2004].

6. Direct Aerosol Radiative Perturbation Estimates

[33] The SW DARP is computed as the difference between the net shortwave radiative flux (between 0.28 and 4.0 μm) at TOA with and without aerosols in clear- and all-sky conditions (Figure 9). For the sake of comparison we

also present estimates over the ocean made from the POLDER-1 (Polarization and Directionality of the Earth's Reflectances) satellite and AERONET observations. These estimates are averaged values for the period 1996–1997 from *Bellouin et al.* [2003]. The spatial features in the POLDER estimates are also seen in the model (left panels) with lower magnitudes especially over the remote oceans. The sign of the SW DARP is determined by aerosol SSA and asymmetry factor, surface albedo, and the average distribution of the solar zenith angle. The estimated clear-sky SW DARP is predominantly negative in all four seasons. There are some patches of positive values over bright surface regions such as Greenland, Antarctica and surrounding sea ice, the Himalayas, and the desertic areas of Australia. Regions with large aerosol loads such as central Africa, east and south Asia, and eastern Europe have the SW DARP in the range of −5 to −10 Wm^{-2}. Remote oceanic regions have the SW DARP between −1 and −5 Wm^{-2}. Seasonal and hemispheric averages of SW DARP are summarized in Table 5. A significant difference with previous studies lies in the sign of the SW DARP over

Figure 10. Seasonally and annually averaged DARP (W m^{-2}) in the longwave spectrum in all-sky conditions from the model. See color version of this figure at back of this issue.

Table 6. Comparison of Published Shortwave DARP (Wm^{-2})

	Clear Sky					All Sky				
Season	NH	SH	Global	Land Only	Ocean Only	NH	SH	Global	Land Only	Ocean Only
This study	−2.78	−1.56	−2.17	−2.01	−2.25	−1.51	−0.58	−1.04	−1.28	−0.93
Jacobson [2001]	–	–	−2.48	–	–	–	–	−1.23		
Takemura et al. [2002]	−1.40	−1.20	−1.30	–	–	−0.17	−0.30	−0.24	–	–
Liao et al. [2004]	–	–	–	–	–	–	–	−0.93[a]	–	–
POLDER [*Bellouin et al.*, 2003]	–	–	–	–	−5.32	–	–	–	–	–

[a]Sum of SW DARP by sulfate, BC, OM, dust, and sea salt only.

the Sahara and Arabia which turns out to be negative if more realistic dust optical properties (i.e., less absorbing) are used. In contrast *Sokolik and Toon* [1996] and *Takemura et al.* [2002] reported positive values for clear-sky SW DARP over the Sahara. On the basis of recent data of the SHADE experiment *Myhre et al.* [2003] also estimated a negative SW DARP for Saharan dust. The globally and annually averaged clear-sky SW DARP is −2.17 Wm^{-2}, with NH and SH average values of −2.78 and −1.56 Wm^{-2}, respectively.

[34] The presence of clouds alters the SW DARP by aerosols. For absorbing aerosols (e.g., BC) the relative altitudes of aerosols and clouds also play an important role as this could change the sign of the forcing [*Haywood and Ramaswamy*, 1998; *Keil and Haywood*, 2003]. The spatial patterns of all-sky SW DARP largely follow those of the clear-sky DARP but with a lower magnitude by a factor of about or less than 2. The globally and annually averaged all-sky SW DARP is −1.04 Wm^{-2}. A striking difference between the clear- and all-sky SW DARP distributions is located off the west coasts of Namibia, Peru, and California, where the SW DARP turns out to be positive in all-sky conditions. These regions are well known for the frequent occurrence of low level stratiform clouds. The positive SW DARP off the coast of Namibia was first predicted by *Keil and Haywood* [2003] based on data from the SAFARI campaign and cloud estimates from ISCCP. They estimated clear- and all-sky SW DARP at −13 and +11.5 Wm^{-2}, respectively. We can certainly conclude that the patches of positive SW DARP over the oceans in our model are plausible.

[35] We estimated the DARP of all aerosols in the long-wave spectrum. The seasonally and annually average LW DARP in all-sky conditions is shown in Figure 10. The global annual average LW DARP in all-sky conditions is +0.45 W m^{-2} from all aerosol species and is a factor of 1.5 smaller than that of in clear-sky conditions. The LW DARP is dominated by mineral dust and have a strong seasonality associated with dust emissions. The other important contributor to the LW DARP is the supermicron sea salt [*Reddy et al.*, 2005].

[36] A comparison of present estimates of SW DARP with other global multicomponent aerosol models is presented in Table 6. The present estimate of clear-sky SW DARP (−2.17 Wm^{-2}) turns out to be in between the estimates of *Takemura et al.* [2002] (−1.30 Wm^{-2}) and *Jacobson* [2001] (−2.48 Wm^{-2}). Our all-sky SW DARP is close to the estimates by *Liao et al.* [2004] and *Jacobson* [2001] but quite different from the estimate of *Takemura et al.* [2002] who predict a very low all-sky to clear-sky ratio.

In the present study aerosols are assumed to consist of an external mixture. In the literature some of the studies assumed an internal mixture in order to estimated the DARP. The difference comes mostly from BC aerosols since BC mass absorption efficiency and DARP are strong functions of the mixing state of BC. The assumption of an internal mixture typically leads to a factor of two larger DARP than that for an external mixture [*Jacobson*, 2001]. The all-sky annual mean SW DARP by BC in our study is +0.53 Wm^{-2}, comparable to the reported range in [*Ramaswamy et al.*, 2001] but lower than the internal mixture estimates of *Jacobson* [2001] and *Liao et al.* [2004].

7. Conclusions

[37] We have carried out a global simulation of the atmospheric cycle of major tropospheric aerosols: sulfate, black carbon, organic matter, mineral dust, and sea salt in the LMDZT GCM. We use seasonal biomass burning emissions inferred from satellite detected fire counts, dust emissions parameterized as a function of soil particle size and clay content, and sea salt emissions as a function of the model 10-m winds. The simulation has been carried out in nudged mode for the years 2000 and 2001 with meteorological fields from ECMWF.

[38] The AOD has been estimated by prescribing RH-dependent aerosol optical properties for hygroscopic aerosols (e.g., sulfate, OM, and sea salt), and updated optical properties for dust and black carbon. Assuming aerosols are present as an external mixture in the atmosphere the total AOD is computed as the sum of AODs by the individual species. Model-predicted AOD is compared with AERONET measurements at various sites. The model reproduces the seasonal cycle of AOD reasonably well. The comparison of model monthly mean AOD (at 500 nm) with data for all available AERONET stations (about 240) shows a correlation coefficient of 0.57 (N = 1324) with 76% of the data points falling within a factor of 2 deviation. If the comparison is done on a daily basis the correlation coefficient drops to 0.49 (N = 23,680) with 65% of the data points falling within a factor of 2 deviation. The model evaluation with monthly mean is encouraging but it seems that assimilation of satellite AOD and fire counts is now needed to improve the model performance on a daily basis. The model underestimates the average AERONET aerosol extinction and absorption optical depths by 22 and 24%, respectively. This contrasts with the study by *Sato et al.* [2003] who report a factor of 2 to 4 underestimation of aerosol absorption by global aerosol models. It is unlikely that our DARP is

underestimated to a larger extent than AODs. A comparison of monthly mean model AOD (550 nm) with MODIS retrievals shows a reasonable agreement, especially in the annual zonal mean. The major differences between the model and satellite AODs are an underestimation of AOD over Asia especially during January to April and over remote regions.

[39] The DARP from all aerosol species has been estimated in SW and LW at TOA in clear- and all-sky conditions. The clear-sky SW DARP forcing at the TOA is predominantly negative and ranges between -5 to -10 Wm^{-2} over aerosol source and outflow regions and -1 to -5 Wm^{-2} over remote regions. The SW DARP in all-sky conditions is similar to that in clear-sky conditions but with a smaller magnitude. The presence of absorbing aerosols (e.g., BC) above cloudy layers also results in positive forcing off the west coasts of Namibia, Peru, and California. In agreement with recent measurements the use of less absorbing optical properties for dust results in negative SW DARP over desert regions. The globally and annually averaged SW DARP in clear-sky conditions (-2.17 Wm^{-2}) is about a factor of 2 larger than in all-sky conditions (-1.04 Wm^{-2}). The LW DARP by all aerosols is estimated to be $+0.71$ and $+0.45$ Wm^{-2}, in clear- and all-sky conditions, respectively. The net DARP (sum of SW and LW) by all aerosols is -1.46 and -0.59 Wm^{-2}, in clear- and all-sky conditions, respectively.

[40] The SW and LW DARP by aerosol species and source types is the subject of a companion paper [*Reddy et al.*, 2005]. An evaluation of the predictive sources for sea salt and dust without nudging is also underway in order to study the response of natural aerosols to future climate change.

References

Anderson, T. L., R. J. Charlson, S. E. Schwartz, R. Knutti, O. Boucher, H. Rodhe, and J. Heintzenberg (2003), Climate forcing by aerosols—A hazy picture, *Science*, *300*, 1103–1104.

Bellouin, N., O. Boucher, D. Tanré, and O. Dubovik (2003), Aerosol absorption over the clear-sky oceans deduced from POLDER-1 and AERONET observations, *Geophys. Res. Lett.*, *30*(14), 1748, doi:10.1029/2003GL017121.

Boucher, O., and T. L. Anderson (1995), GCM assessment of the sensitivity of direct climate forcing by anthropogenic sulfate aerosols to aerosol size and chemistry, *J. Geophys. Res.*, *100*, 26,117–26,134.

Boucher, O., and M. Pham (2002), History of sulfate aerosol radiative forcings, *Geophys. Res. Lett.*, *29*(9), 1308, doi:10.1029/2001GL014048.

Boucher, O., M. Pham, and C. Venkataraman (2002), Simulation of the atmospheric sulfur cycle in the Laboratoire de Météorologie Dynamique general circulation model: Model description, model evaluation, and global and European budgets, *Note Sci. IPSL 23*, 27 pp., Inst. Pierre Simon Laplace, Paris. (Available at http://www.ipsl.jussieu.fr/poles/Modelisation/NotesSciences.htm.)

Chin, M., P. Ginoux, S. Kinne, O. Torres, B. Holben, B. Duncan, R. Martin, J. Logan, A. Higurashi, and T. Nakajima (2002), Tropospheric aerosol optical thickness from the GOCART model and comparisons with satellite and sunphotometer measurements, *J. Atmos. Sci.*, *59*, 461–483.

Chu, D. A., Y. Kaufman, C. Ichoku, L. A. Remer, D. Tanré, and B. Holben (2002), Validation of MODIS aerosol optical depth retrieval over land, *Geophys. Res. Lett.*, *29*(12), 8007, doi:10.1029/2001GL013205.

Chuang, C. C., J. E. Penner, J. M. Prospero, K. E. Grant, G. H. Rau, and K. Kawamoto (2002), Cloud susceptibility and the first aerosol indirect forcing: Sensitivity to black carbon and aerosol concentrations, *J. Geophys. Res.*, *107*(D21), 4564, doi:10.1029/2000JD000215.

Clarke, A., V. Kapustin, W. Collins, P. Rasch, K. Moore, S. Howell, and H. Fuelberg (2001), Dust and pollution transport on global scales: Aerosol measurements and model predictions, *J. Geophys. Res.*, *106*, 32,555–32,569.

Cooke, W. F., and J. J. N. Wilson (1996), A global black carbon aerosol model, *J. Geophys. Res.*, *101*, 19,395–19,409.

Cooke, W. F., C. Liousse, H. Cachier, and J. Feichter (1999), Construction of a 1° × 1° fossil fuel emission data set for carbonaceous aerosol and implementation and radiative impact in the ECHAM4 model, *J. Geophys. Res.*, *104*, 22,137–22,162.

Dubovik, O., B. Holben, T. F. Eck, A. Smirnov, Y. J. Kaufman, M. D. King, D. Tanré, and I. Slutsker (2002), Variability of absorption and optical properties of key aerosol types observed in worldwide locations, *J. Atmos. Sci.*, *59*, 590–608.

Fouquart, Y., and B. Bonnel (1980), Computations of solar heating of the Earth's atmosphere: A new parameterization, *Beitr. Phys. Atmos.*, *53*, 35–63.

Giorgi, F., and W. L. Chameides (1986), Rainout lifetimes of highly soluble aerosols and gases as inferred from simulations with a general circulation model, *J. Geophys. Res.*, *91*, 14,367–14,376.

Gong, S. L., et al. (2003), Canadian Aerosol Module: A size-segregated simulation of atmospheric aerosol processes for climate and air quality models: 1. Module development, *J. Geophys. Res.*, *108*(D1), 4007, doi:10.1029/2001JD002002.

Guelle, W., Y. J. Balkanski, M. Schulz, B. Marticorena, H. Bergametti, C. Moulin, R. Arimoto, and K. D. Perry (2000), Modeling the atmospheric distribution of mineral aerosol: Comparison with ground measurements and satellite observations for yearly and synoptic timescales over the North Atlantic, *J. Geophys. Res.*, *105*, 1997–2012.

Guenther, A., et al. (1995), A global model of natural volatile organic compound emissions, *J. Geophys. Res.*, *100*, 8873–8892.

Hauglustaine, D. A., F. Hourdin, L. Jourdain, M.-A. Filiberti, S. Walters, J.-F. Lamarque, and E. A. Holland (2004), Interactive chemistry in the Laboratoire de Météorologie Dynamique general circulation model: Description and background tropospheric chemistry evaluation, *J. Geophys. Res.*, *109*, D04314, doi:10.1029/2003JD003957.

Haywood, J. M., and V. Ramaswamy (1998), Global sensitivity studies of the direct radiative forcing due to anthropogenic sulfate and black carbon aerosols, *J. Geophys. Res.*, *103*, 6043–6058.

Haywood, J. M., and K. P. Shine (1995), The effect of anthropogenic sulfate and soot aerosol on the clear sky planetary radiation budget, *Geophys. Res. Lett.*, *22*, 603–605.

Haywood, J., P. Francis, S. Osborne, M. Glew, N. Loeb, E. Highwood, D. Tanré, G. Myhre, P. Formenti, and E. Hirst (2003), Radiative properties and direct radiative effect of Saharan dust measured by the C-130 aircraft during SHADE: 1. Solar spectrum, *J. Geophys. Res.*, *108*(D18), 8577, doi:10.1029/2002JD002687.

Higurashi, A., T. Nakajima, B. N. Holben, A. Smirnov, R. Frouin, and B. Chatenet (2000), A study of global aerosol optical climatology with two-channel AVHRR remote sensing, *J. Clim.*, *13*, 2011–2027.

Hourdin, F., and A. Armangaud (1999), The use of finite-volume methods for atmospheric advection of trace species. Part I: Test of various formulations in a general circulation model, *Mon. Weather Rev.*, *127*, 822–837.

Intergovernmental Panel on Climate Change (IPCC) (2001), *Climate Change 2001: The Scientific Basis, Contribution of Working Group I to the Third Assessment Report of the Intergovernmental Panel on Climate Change*, edited by J. T. Houghton et al., 944 pp., Cambridge Univ. Press, New York.

Jacobson, M. Z. (2001), Global direct radiative forcing due to multicomponent anthropogenic and natural aerosols, *J. Geophys. Res.*, *106*, 1551–1568.

Kaufman, Y. J., D. Tanré, O. Dubovik, A. Karnieli, and L. A. Remer (2001), Absorption of sunlight by dust as inferred from satellite and ground-based remote sensing, *Geophys. Res. Lett.*, *28*, 1479–1482.

Keil, A., and J. M. Haywood (2003), Solar radiative forcing by biomass burning aerosol particles during SAFARI 2000: A case study based on measured aerosol and cloud properties, *J. Geophys. Res.*, *108*(D13), 8467, doi:10.1029/2002JD002315.

Köpke, P., M. Hess, I. Schult, and E. P. Shettle (1997), Global aerosol data set, *Tech. Rep. 243*, pp. 103–158, Max-Planck-Inst. für Meteorol., Hamburg.

Liao, H., J. H. Seinfeld, P. J. Adams, and L. J. Mickley (2004), Global radiative forcing of coupled tropospheric ozone and aerosols in a unified general circulation model, *J. Geophys. Res.*, *109*, D16207, doi:10.1029/2003JD004456.

Liousse, C., J. E. Penner, C. Chuang, J. J. Walton, H. Eddleman, and H. Cachier (1996), A global three-dimensional model study of carbonaceous aerosols, *J. Geophys. Res.*, *101*, 19,411–19,432.

Monahan, E. C., D. E. Spiel, and K. L. Davidson (1986), *A Model of Marine Aerosol Generation via Whitecaps and Wave Disruption, in Oceanic Whitecaps*, edited by E. C. Monahan and G. Mac Niocail, pp. 167–174, Springer, New York.

Morcrette, J.-J. (1991), Radiation and cloud radiative properties in the European Centre for Medium-Range Weather Forecasts forecasting systems, *J. Geophys. Res.*, *96*, 9121–9132.

Morcrette, J.-J., and Y. Fouquart (1986), The overlapping of cloud layers in shortwave radiation parameterizations, *J. Atmos. Sci.*, *43*, 321–328.

Myhre, G., A. Grini, J. M. Haywood, F. Stordal, B. Chatenet, D. Tanré, J. K. Sundet, and I. S. A. Isaksen (2003), Modeling the radiative impact of mineral dust during the Saharan Dust Experiment (SHADE) campaign, *J. Geophys. Res.*, *108*(D18), 8579, doi:10.1029/2002JD002566.

Myhre, G., et al. (2004), Intercomparison of satellite retrieved aerosol optical depth over the ocean, *J. Atmos. Sci.*, *61*, 499–513.

O'Dowd, C. D., B. Davison, J. A. Lowe, M. H. Smith, R. M. Harrison, and C. N. Hewitt (1997), Biogenic sulphur emissions and inferred sulphate CCN concentrations in and around Antarctica, *J. Geophys. Res.*, *102*, 12,839–12,854.

Olivier, J. G. J., and J. J. M. Berdowski (2001), Global emissions sources and sinks, in *The Climate System*, edited by J. Berdowski, R. Guicherit, and B. J. Heij, pp. 33–78, A. A. Balkema, Brookfield, Vt.

Pandis, S. N., S. E. Paulson, J. H. Seinfeld, and R. C. Flagan (1991), Aerosol formation in the photooxidation of isoprene and beta-pinene, *Atmos. Environ. Part A*, *25*, 997–1008.

Penner, J. E., et al. (2002), A comparison of model- and satellite-derived aerosol optical depth and reflectivity, *J. Atmos. Sci.*, *59*, 441–460.

Pham, M., J.-F. Müller, G. P. Brasseur, C. Granier, and G. Mégie (1996), A 3D model study of the global sulphur cycle: Contributions of anthropogenic and biogenic sources, *Atmos. Environ.*, *30*, 1815–1822.

Ramaswamy, V., O. Boucher, J. Haigh, D. Hauglustaine, J. Haywood, G. Myhre, T. Nakajima, G. Y. Shi, and S. Solomon (2001), Radiative forcing of climate change, in *Climate Change 2001, The Scientific Basis, Contribution of Working Group I to the Third Assessment Report of the IPCC*, edited by J. T. Houghton et al., chap. 6, pp. 349–416, Cambridge Univ. Press, New York.

Reddy, M. S., and O. Boucher (2004), A study of the global cycle of carbonaceous aerosols in the LMDZT general circulation model, *J. Geophys. Res.*, *109*, D14202, doi:10.1029/2003JD004048.

Reddy, M. S., O. Boucher, C. Venkataraman, S. Verma, J.-F. Léon, N. Bellouin, and M. Pham (2004), General circulation model estimates of aerosol transport and radiative forcing during the Indian Ocean Experiment, *J. Geophys. Res.*, *109*, D16205, doi:10.1029/2004JD004557.

Reddy, M. S., O. Boucher, Y. Balkanski, and M. Schulz (2005), Aerosol optical depths and direct radiative perturbations by species and source type, *Geophys. Res. Lett.*, doi:10.1029/2004GL021743, in press.

Remer, L. A., et al. (2002), Validation of MODIS aerosol retrieval over ocean, *Geophys. Res. Lett.*, *29*(12), doi:10.1029/2001GL013204.

Sato, M., J. Hansen, D. Koch, A. Lacis, R. Ruedy, O. Dubovik, B. Holben, M. Chin, and T. Novakov (2003), Global atmospheric black carbon inferred from AERONET, *Proc. Natl. Acad. Sci.*, *100*, 6319–6324.

Schulz, M., Y. Balkanski, F. Dulac, and W. Guelle (1998), Role of aerosol size distribution and source location in a three-dimensional simulation of a Saharan dust episode tested against satellite-derived optical thickness, *J. Geophys. Res.*, *103*, 10,579–10,592.

Sokolik, I. N., and O. B. Toon (1996), Direct radiative forcing by anthropogenic airborne mineral aerosols, *Nature*, *381*, 681–683.

Takemura, T., T. Nakajima, O. Dubovik, B. N. Holben, and S. Kinne (2002), Single-scattering albedo and radiative forcing of various aerosol species with a global three-dimensional model, *J. Clim.*, *15*, 333–352.

Tang, I. N. (1997), Thermodynamic and optical properties of mixed-salt aerosols of atmospheric importance, *J. Geophys. Res.*, *102*, 1883–1893.

Tang, I. N., and H. R. Munkelwitz (1994), Water activities, densities, and refractive indices of aqueous sulfates and sodium nitrate droplets of atmospheric importance, *J. Geophys. Res.*, *99*, 18,801–18,808.

Tegen, I., P. Hollrig, M. Chin, I. Fung, D. Jacob, and J. Penner (1997), Contribution of different aerosol species to the global aerosol extinction optical thickness: Estimates from model results, *J. Geophys. Res.*, *102*, 23,895–23,915.

Tiedtke, M. (1989), A comprehensive mass flux scheme for cumulus parameterization in large-scale models, *Q. J. R. Meteorol. Soc.*, *117*, 1779–1800.

Tsigaridis, K., and M. Kanakidou (2003), Global modelling of secondary organic aerosol in the troposphere: A sensitivity analysis, *Atmos. Chem. Phys.*, *3*, 1849–1869.

Turpin, B. J., and H.-J. Lim (2002), Species contributions to PM2. 5 mass concentrations: Revisiting common assumptions for estimating organic mass, *Aerosol Sci. Technol.*, *35*, 602–610.

van Leer, B. (1977), Towards the ultimate conservative difference scheme: IV. A new approach to numerical convection, *J. Comput. Phys.*, *23*, 276–299.

Volz, F. (1973), Infrared optical constants of ammonium sulfate, Sahara dust, volcanic pumice, and flyash, *Appl. Opt.*, *12*, 564–568.

————————————

Y. Balkanski and M. Schulz, Laboratoire des Sciences, Climat et de l'Environnement, L'Orme des Merisiers, Bat 709, F-91191 Gif-sur-Yvette, France. (balkanski@lsce.saclay.cea.fr; schulz@lsce.saclay.cea.fr)

N. Bellouin, O. Boucher, and M. S. Reddy, Laboratoire d'Optique Atmosphérique, CNRS, Université des Sciences et Technologies de Lille, F-59655 Villeneuve d'Ascq, France. (bellouin@loa.univ-lille1.fr; boucher@loa.univ-lille1.fr; reddy@loa.univ-lille1.fr)
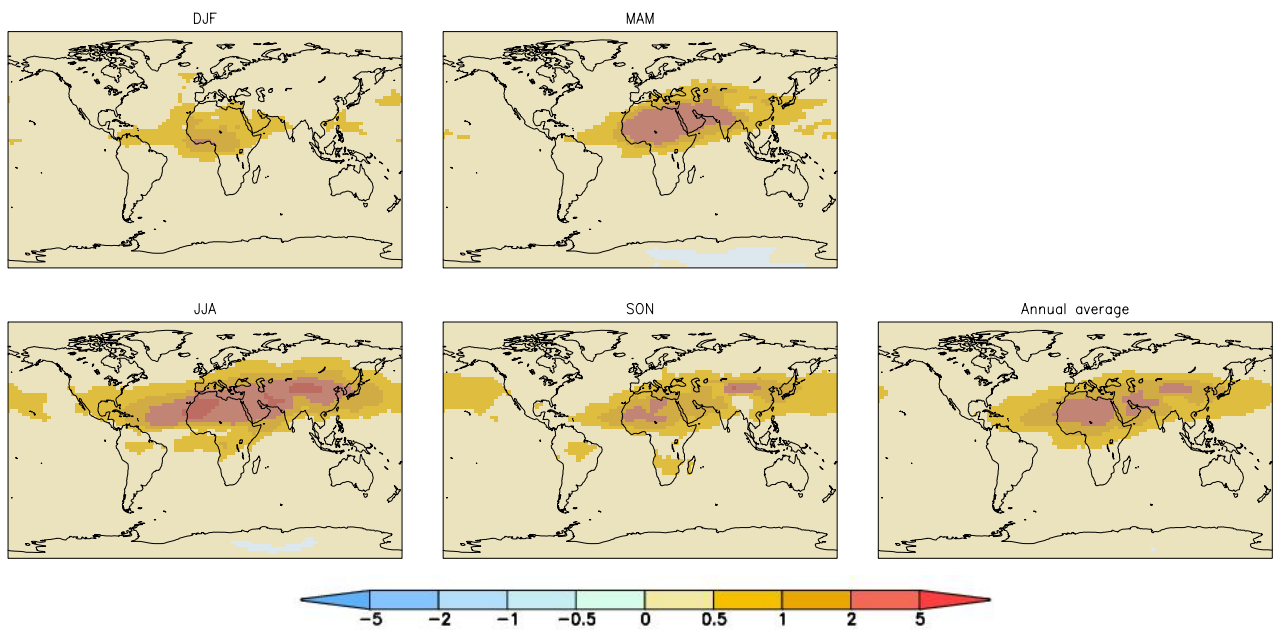
J.-L. Dufresne, Laboratoire de Météorologie Dynamique, CNRS, Université Paris 6, 4 Place Jussieu, F-75252 Paris Cedex 05, France. (jean-louis.dufresne@lmd.jussieu.fr)

M. Pham, Service d'Aéronomie, Boîte 102, Université Pierre et Marie Curie, 4 Place Jussieu, F-75252 Paris Cedex 05, France. (pham@aero.jussieu.fr)
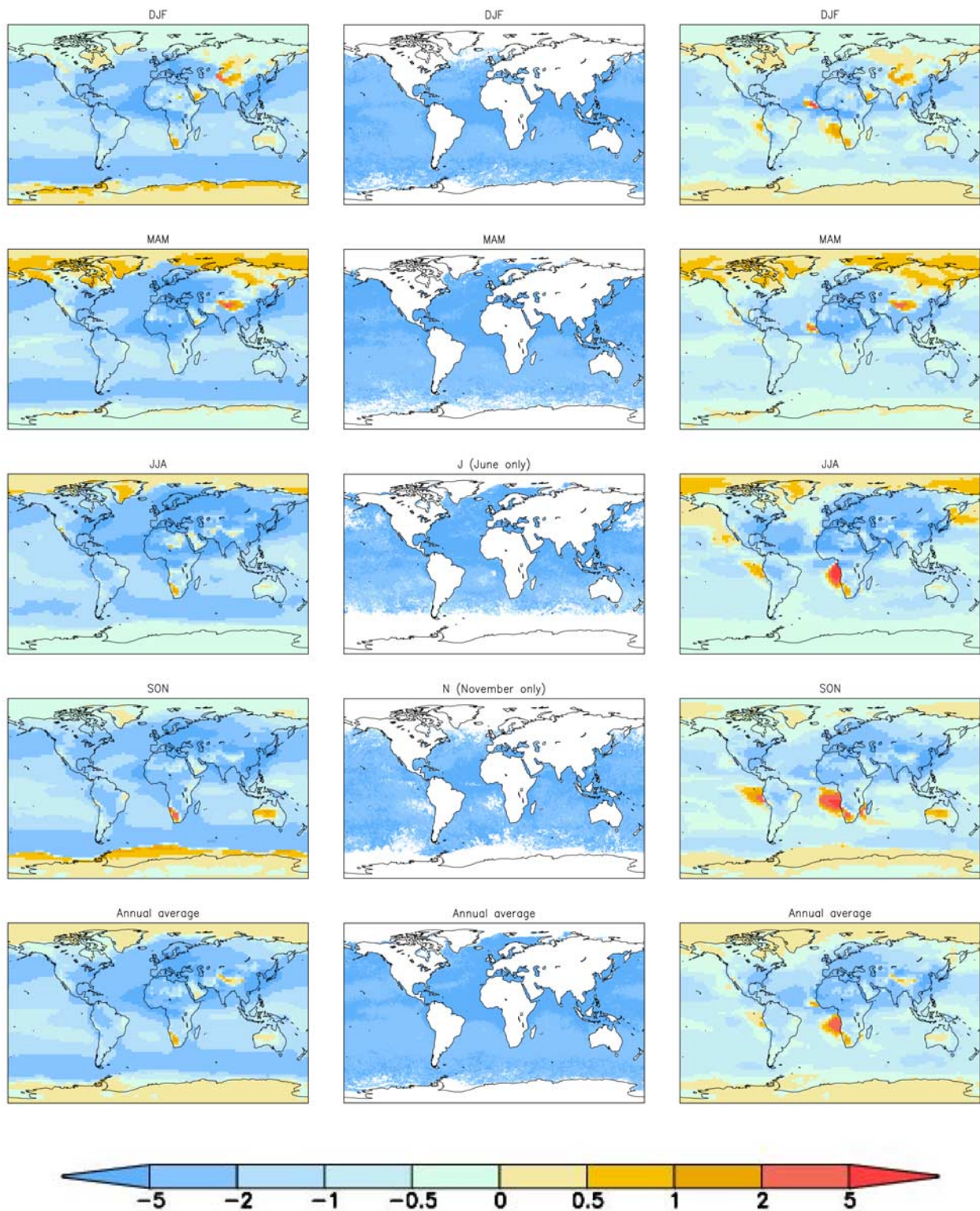
Figure 9. Seasonally and annually averaged DARP (W m^{-2}) in the shortwave spectrum in clear-sky conditions from the model (left panels) and from POLDER (middle panels), and in all-sky conditions from the model (right panels).

Figure 10. Seasonally and annually averaged DARP (W m^{-2}) in the longwave spectrum in all-sky conditions from the model.